Engineering Journal issn: 0125-8281

Article

Development of Stress-Based Forming Limit Curves for Predicting Crack Occurred during Deformation of UHSS DP980's Parts

Chanatip Tonglamool[a] **and Surasak Suranuntchai**[b,*]

Department of Tool and Materials Engineering, Faculty of Engineering, King Mongkut's University of Technology Thonburi, Bangkok 10140, Thailand
E-mail: [a]chanatip.t@mail.kmutt.ac.th, [b,*]surasak.sur@kmutt.ac.th (Corresponding author)

Abstract. Unless the strain-based forming limit diagram (ε-FLD) is a useful tool in failure prediction for sheet metal, the complex shape can lead to a non-linear strain history, which ε-FLD cannot adequately describe. This issue can be improved by using the stress-based forming limit diagram (σ-FLD). However, determining the σ-FLD through direct theoretical calculation is complex for beginners. This research uses a forming simulation software named PAM-STAMP to transform ε-FLD to σ-FLD by simulating the Nakajima stretch test. Because a yield criterion and hardening model are required in σ-FLD determining procedures, this research also studies the accuracy of Hill48, Barlat89, and Yld2000 (in the absence of balanced biaxial condition test results) when integrated with the Swift hardening model and the Yoshida-Uemori (Y-U) model. The thickness and springback of an automotive part named Panel-RF FRT HRD were used to compare the accuracy of the forming simulation. It was found that the σ-FLD predicted a crack on the workpiece better than the ε-FLD, no matter whether there were differences in combination in yield criteria or hardening models. In the thickness and springback prediction, the r-based Hill48 couple Y-U model showed the best result, followed by Barlat89 and Yld2000, and was less accurate when Hill48 was coupled with the Swift hardening model.

Keywords: Stress-based forming limit diagram, high-strength steel, surface crack, springback, finite element.

ENGINEERING JOURNAL Volume 28 Issue 9
Received 26 March 2024
Accepted 13 September 2024
Published 30 September 2024
Online at https://engj.org/
DOI:10.4186/ej.2024.28.9.51

DOI:10.4186/ej.2024.28.9.51

1. Introduction

According to the emission standards, the automobile industry has adapted to the use of high-strength-to-weight ratio materials to reduce vehicle weight. While aluminum is famous for its lightweight properties, high-strength steel remains an appropriate choice for the automotive industry due to its lower cost and better formability compared to aluminum. However, the formability of high-strength steel is lower than conventional steel due to a strong microstructure like martensite. A large deformation or sharp bending could lead to a visible crack. The diagrams of Keeler and Goodwin [1], also known as the strain-based forming limit diagram (ε-FLD), is an essential tool along with the forming simulation software in failure prediction. Because it mainly covers failure prediction in both stamping and deep drawing processes, unless working with a multi-step forming or pre-strain workpiece could make ε-FLD mispredict failures because the strain history exhibits a nonconstant ratio between principal strains [2] . For this reason, other types of failure criteria have been introduced to reduce the limitations of ε-FLD.

Instead of using the principal strain relation, Arrieux et al. [3] introduced the failure criteria that rely on principal stress, called the stress-based forming limit diagram or σ-FLD. The method to determine the σ-FLD proposed by Arrieux et al. [3] is the conversion of the principal strain relation in the ε-FLD to the principal stress relation by calculating an increment of strain under the assumption of Hill48 yield function, Hollomon's hardening model, and the Levy-Mises flow rule. First, the ε-FLD was determined by the Nakajima stretch test. Then, calculate the change in stress following the strain history from the initial stage to reach the forming limit curve (FLC). However, calculating the change in principle stress following the strain history is complex. Uthaisangsuk et al. [2] suggest using the finite element method via Abaqus software to calculate the change in principal stress to reduce complex calculations. At this point, the yield criteria and hardening models become significant factors for determining σ-FLD because they represent the material's behavior during simulation. Variations in yield criteria or hardening models can alter the calculation result of the principal stresses in the σ-FLD determining process, as observed in the works of Butuc et al. [4], Panich et al. [5], and Nakwattanaset et al. [6].

The primary role of the yield criterion in forming a simulation is to express the states of stress that will cause elastic deformation to become plastic deformation [7] and to describe thinning behavior. Since steel sheets are anisotropic materials, yield criteria from Hill's family (Hill48 and Hill90) and Hershey's family (Barlat89, Yld2000, and BBC 2005) are optimal choices in commercial finite element software for anisotropic materials. The fewer required mechanical parameters for the Hill48 and Barlat89 yield criteria make them more convenient to apply than the Yld2000 and BBC2005. However, an estimation of uniaxial yield stresses and Lankford coefficients (r-value) in variation angle to the rolling direction (RD) by Hill48 and Barlat89 shows that they are uncorrelated to the experimental results except for Yld2000, which appear in [8-12]. In Yld2000, the yield stress and r-value in balanced biaxial conditions are needed to determine the yield function's anisotropy coefficients. The yield stress and r-value in balanced biaxial conditions can be obtained by performing a cruciform test for both yield stress and r-value or an individual test: a bulge test for yield stress and a disk compression test for r-value.

Hardening laws work alongside yield functions to express the strain-hardening effect after the stress exceeds the yield condition [7] and play an important role in springback prediction. High-strength steel has more than just formability issues; springback is also a concern in the automotive industry because it directly affects product dimensions, resulting in an assembly part conflict. This phenomenon results from the remaining stress in the elastic deformation region resisting the plastic deformation region in the forming area, especially in thin material. Research by Ghaei et al. [13] indicates another cause of springback is the difference in elastic modulus in loading and unloading conditions, which also shows that the elastic modulus has lowered in the unloading stages. Consequently, the constant modulus procedure in the isotropic hardening laws could give a less accurate result. For better results in springback prediction, Chongthairungruang et al. [14], Uemori et al. [15], and Julsri et al. [16] suggest the mixed kinematic hardening name Yoshida-Uemori [17] (Y-U) model. The benefits of this model cover the most common behaviors of steel sheets, such as decaying modulus, the Bauschinger effect, the transient Bachinger effect, and workhardening stagnation. While the Y-U model is widely used in springback prediction, the complexity of this model, combined with the recent yield criteria to make σ-FLD, could take time to develop the VUMAT subroutine in Abaqus for beginners.

As mentioned earlier, the Yld2000 yield function is excellent for predicting material behavior because it requires more mechanical properties to calibrate the anisotropy coefficients compared to Hill48 and Barlat89. However, mechanical properties under biaxial conditions require specific tools. When experiments under biaxial conditions cannot be performed, many scholars approximate mechanical properties under biaxial conditions. For instance, Brinis et al. [18] assumed that the balanced biaxial yield stress was equal to the yield stress from the RD. Lee et al. [19]. and Hou et al. [20]. used the average uniaxial tension yield stress in three directions to represent the balanced biaxial yield stress. The r-value under balanced biaxial conditions can be calculated using the Yld96 or polycrystal model, as suggested by Barlat et al. [21], and this approach has also been used by Hou et al. [20] and Chahaoui et al. [22]. Although two different methods for estimating the yield

stress under biaxial conditions allow for the study of Yld2000's characteristics, the most appropriate method for industrial applications has yet to be determined.

This research aims to improve the prediction ability of ε-FLD by transforming it to σ-FLD using the simulation of the Nakajima stretch test via the sheet metal forming simulation software named PAM-STAMP. The visible surface crack on the automotive part named Panel-RF FRT HRD is used to verify the predictive ability of the crack prediction between σ-FLD and ε-FLD. Since yield functions and hardening models are the primary variables in σ-FLD determination, this study also investigates the various combinations of yield functions and hardening models that are suitable for representing the NSC980D steel behavior under the following topics: thinning and springback.

2. Material Models

2.1. Yield Function

2.1.1. Hill 1948

Hill [23] proposed the yield function Hill48 in 1948. This model is an improvement from Huber-Mises by integrating six coefficients into Eq. (1) to create anisotropy conditions that make Hill48 the first yield function for anisotropic materials such as rolled sheets. The Hill48 yield function is expressed in Eq. (2).

$$2f_y(\sigma_{ij}) = (\sigma_{xx}-\sigma_{yy})^2 + (\sigma_{yy}-\sigma_{zz})^2 + (\sigma_{zz}-\sigma_{xx})^2 + 6(\sigma_{xy}^2+\sigma_{yz}^2+\sigma_{zx}^2) \quad (1)$$

$$2f_y(\sigma_{ij}) = F(\sigma_{yy}-\sigma_{zz})^2 + G(\sigma_{zz}-\sigma_{xx})^2 + H(\sigma_{xx}-\sigma_{yy})^2 + 2L\sigma_{yz}^2 + 2M\sigma_{zx}^2 + 2N\sigma_{xy}^2 \quad (2)$$

where $\bar{\sigma}$ and σ_{ij} (i, j = x, y, z) are the equivalent stress and stress tensor. F, G, H, L, M, and N are the anisotropy coefficient. When the plane stress condition (σ_{zz}=σ_{yz}=σ_{zx}=0) is considered, Eq. (2) is reduced to the following equation:

$$2f_y(\sigma_{ij}) = (G+H)\sigma_{xx}^2 - 2H\sigma_{xx}\sigma_{yy} + (H+F)\sigma_{yy}^2 + 2N\sigma_{xy}^2 \quad (3)$$

Three methods can be used to obtain the four anisotropy coefficients (F, G, H, and N) [24]. One well-known method is the r-based method, which uses the r-value from three directions, as illustrated in Eq. (4)

$$F = \frac{2r_0}{r_{90}(1+r_0)} \qquad G = \frac{2}{1+r_0}$$
$$H = \frac{2r_0}{1+r_0} \qquad N = \frac{2(1+2r_{45})(r_0+r_{90})}{2r_{90}(1+r_0)} \quad (4)$$

r_0, r_{45}, and r_{90} denote the experimental data of the r-value in uniaxial tension in the direction, making an angle of 0, 45, and 90 degrees to the RD.

2.1.2. Barlat 1989

Barlat and Lian [25] proposed the Barlat89 yield function in 1989. It was developed from the previous work of Barlat and Richmond [26], which was initially a plane stress isotropic yield function based on crystal plasticity, as shown in Eq. (5). After, Barlat and Lian [25] integrated four coefficients, a, c, h, and p, into Eq. (5), which makes Barlat89 able to describe the anisotropy case. The Barlat89 equation is expressed in Eq. (6).

$$f_y(\sigma_{ij}) = |K_1+K_2|^m + |K_1-K_2|^m + |2K_2|^m = 2\bar{\sigma}^m \quad (5)$$

$$f_y(\sigma_{ij}) = a|K_1+K_2|^m + a|K_1-K_2|^m + c|2K_2|^m = 2\bar{\sigma}^m \quad (6)$$

where

$$K_1 = \frac{\sigma_{xx}+h\sigma_{yy}}{2}$$
$$K_2 = \sqrt{\left(\frac{\sigma_{xx}-h\sigma_{yy}}{2}\right)^2 + (p\sigma_{xy})^2} \quad (7)$$

From the above equation, m is the exponent determined by the crystallographic structure of the material: for BCC, m = 6; for FCC, m = 8. The parameters a, c, h, and p are anisotropy coefficients that can be identified using stress-based or r-value-based methods [27]. When the r-value is used to calibrate the anisotropy coefficients, this yield function might be called the Barlat 3-parameter yield function because three r-values in different uniaxial directions are required for calibration. The equations for determining anisotropy coefficients by the r-value-based method are illustrated in Eqs. (8-9).

$$a = 2 - 2\sqrt{\frac{R_0R_{90}}{(1+R_0)(1+R_{90})}} \qquad c = 2-a$$
$$h = \sqrt{\frac{R_0(1+R_{90})}{R_{90}(1+R_0)}} \quad (8)$$

The p is a final parameter that can be calculated iteratively from the following equation [25]:

$$r_\theta = \frac{2m\bar{\sigma}^m}{(\frac{\partial f}{\partial\sigma_{xx}}+\frac{\partial f}{\partial\sigma_{yy}})\sigma_\theta} - 1 \quad (9)$$

where r_θ and σ_θ are the experimental data of r-value and yield stress in uniaxial tension in the direction making an angle θ with the RD.

2.1.3. Yld96

Barlat et al. [28] proposed the Yld96 yield function in 1997. This yield function is based on crystal plasticity. They used linear transformation methodology

transition between the anisotropic and isotropic cases, as in the Karafillis and Boyce [29] work. Also, they added three weight factors to their yield function to adjust yield surface prediction. As a result, at least seven mechanical tests are required to define the anisotropy coefficient of this yield function. The Yld96 yield function is expressed in the following form [28]:

$$f_y(\sigma_{ij}) = \alpha_1|S_2 - S_3|^m + \alpha_2|S_3 - S_1|^m + \alpha_3|S_1 - S_2|^m = 2\bar{\sigma}^m \quad (10)$$

where S_1, S_2, and S_3 are the principal deviatoric stresses; α_1, α_2, and α_3 are weight factors that describe the anisotropy of the material. The linear transformation, according to the Karafillis-Boyce yield function, is expressed in the following form [28]:

$$S_{ij} = L\sigma_{ij} \quad (11)$$

where S_{ij} (i, j = x, y) is the component of the isotropic plasticity equivalent stress tensor. L is a linear operator. m is the exponent determined in the same manner as in Barlat89. For orthotopic material under plane stress conditions, all components in Eq. (11) are summarized in the following matrix[28]:

$$\begin{bmatrix} S_{xx} \\ S_{yy} \\ S_{zz} \\ S_{xy} \end{bmatrix} = \begin{bmatrix} \frac{c_2+c_3}{3} & \frac{-c_3}{3} & \frac{-c_2}{3} & 0 \\ \frac{-c_3}{3} & \frac{c_1+c_3}{3} & \frac{-c_1}{3} & 0 \\ \frac{-c_2}{3} & \frac{-c_1}{3} & \frac{c_1+c_2}{3} & 0 \\ 0 & 0 & 0 & c_6 \end{bmatrix} \begin{bmatrix} \sigma_{xx} \\ \sigma_{yy} \\ 0 \\ \sigma_{xy} \end{bmatrix} \quad (12)$$

where c_1, c_2, c_3, and c_6 are anisotropy coefficients that describe the anisotropic of the material. The S_1, S_2, and S_3 that given in Eq. (10) are computed as follows:

$$S_{1,2} = \frac{S_{xx}+S_{yy}}{2} \pm \sqrt{\left(\frac{S_{xx}+S_{yy}}{2}\right)^2 + {S_{xy}}^2}$$
$$S_3 = -S_1 - S_2 \quad (11)$$

Also α_1, α_2, and α_3 that given in Eq. (10) are computed as follows:

$$\alpha_1 = \alpha_x\, cos^2\,\beta + \alpha_y \sin^2\beta$$
$$\alpha_2 = \alpha_x \sin^2\beta + \alpha_y \cos^2\beta \quad (14)$$
$$\alpha_3 = \alpha_{z0} \cos^2 2\beta + \alpha_{z1} \sin^2 2\beta$$

where

$$\alpha_{z0} = 1\ and\ 2\beta = \tan^{-1}\left(\frac{2S_{xy}}{S_{xx}-S_{yy}}\right) \quad (15)$$

The determination method for the seven anisotropy coefficients (c_1, c_2, c_3, c_6, a_x, a_y, and a_{z1}) is given in Appendix A. This yield function can be used for the purpose of predicting the r-value in the balanced biaxial condition. The equation is given by Barlat et al. [30] as shown below.

$$(r_b)_{theory} = \frac{\begin{bmatrix} -\alpha_x(c_3+2c_1)(2c_1+c_2)|2c_1+c_2|^{m-2} \\ +\alpha_y(c_3-c_1)(c_1+2c_2)|c_1+2c_2|^{m-2} \\ -(2c_3+c_1)(c_1-c_2)|c_1-c_2|^{m-2} \end{bmatrix}}{\begin{bmatrix} -\alpha_x(c_2-c_3)(2c_1+c_2)|2c_1+c_2|^{m-2} \\ -\alpha_y(2c_2+c_3)(c_1+2c_2)|c_1+2c_2|^{m-2} \\ +(c_2+2c_3)(c_1-c_2)|c_1-c_2|^{m-2} \end{bmatrix}} \quad (16)$$

2.1.4. Yld2000

The Yld2000 yield function was proposed in 2003 by Barlat et al. [21], they aim to improve the convexity of the yield surface from a previous work named the Yld96 yield function. In this yield function, they use a combination of two isotropic yield functions based on crystal plasticity equipped with the first and second linear transformations, respectively. The linear transformation makes an anisotropic response to yield function by adding the difference weight coefficient to the components of the stress deviator. The total weight coefficient for two linear transformations is expressed by eight coefficients: α_1, α_2, α_3, α_4, α_5, α_6, α_7, and α_8. The eight anisotropy coefficients can be obtained from eight mechanical tests consisting of yield stress and r-value in 3 uniaxial tension directions and balance biaxial tension. The Yld2000 yield function is expressed in the following form [21]:

$$f_y(\sigma_{ij}) = |S_1' - S_2'|^m + |2S_2'' + S_1''|^m + |2S_1'' + S_2''|^m = 2\bar{\sigma}^m \quad (17)$$

where S_i' and S_i'' (i = 1, 2) are the principal values of the transformed stress deviator, and m is the exponent determined in the same manner as Barlat 89. The S_i', S_i'' are computed as follows:

$$S_{1,2}' = \frac{1}{2}\left(S_{xx}' + S_{yy}'\sqrt{\left(S_{xx}' - S_{yy}'\right)^2 + \left(4S_{xy}'\right)^2}\right)$$
$$S_{1,2}'' = \frac{1}{2}\left(S_{xx}'' + S_{yy}''\sqrt{\left(S_{xx}'' - S_{yy}''\right)^2 + \left(4S_{xy}''\right)^2}\right) \quad (18)$$

S_{ij}' and S_{ij}'' (i, j = x, y) are the components of S_i' and S_i'', respectively.

$$S_{ij}' = L'.\sigma_{ij}$$
$$S_{ij}'' = L''.\sigma_{ij} \quad (19)$$

where L', L'' are linear transformations with weight coefficient. The coefficient of L', L'' are given below.

$$\begin{bmatrix} L_{11}' \\ L_{12}' \\ L_{21}' \\ L_{22}' \\ L_{66}' \end{bmatrix} = \frac{1}{3}\begin{bmatrix} 2 & 0 & 0 \\ -1 & 0 & 0 \\ 0 & -1 & 0 \\ 0 & 2 & 0 \\ 0 & 0 & 3 \end{bmatrix} \begin{bmatrix} \alpha_1 \\ \alpha_2 \\ \alpha_7 \end{bmatrix} \quad (20)$$

$$\begin{bmatrix} L''_{11} \\ L''_{12} \\ L''_{21} \\ L''_{22} \\ L''_{66} \end{bmatrix} = \frac{1}{9}\begin{bmatrix} -2 & 2 & 8 & -2 & 0 \\ 1 & -4 & -4 & 4 & 0 \\ 4 & -4 & -4 & 1 & 0 \\ -2 & 8 & 2 & -2 & 0 \\ 0 & 0 & 0 & 0 & 9 \end{bmatrix}\begin{bmatrix} \alpha_3 \\ \alpha_4 \\ \alpha_5 \\ \alpha_6 \\ \alpha_8 \end{bmatrix}$$

The determination method for the eight anisotropy coefficients (α_1 to α_8) is given in Appendix B.

2.2. Hardening Models

2.2.1. Swift hardening model

The Swift hardening model is one of the isotropic hardening laws. The benefit of this equation is that it gives more flexibility in curve fitting than the Hollomon equation because of an extra parameter. The Swift equation is given by.

$$\bar{\sigma} = K(\varepsilon_0 + \varepsilon_p)^n \tag{21}$$

where $\bar{\sigma}$ and ε_p are effective stress and plastic strain, K, ε_0, and n are material parameters. The Swift function coefficient can be obtained by curve fitting the stress-strain curve from the uniaxial tensile test.

2.2.2. Yoshida-Uemori (Y-U)

The Y-U model was proposed by Yoshida and Uemori [17] in 2002. This hardening model is constructed based on the two-surface plasticity theory from Krieg [31] work. The outer surface is named the bounding surface (F), generated from mixed hardening laws for expressing global workhardening. The inner surface is named the yield surface (f), generated from nonlinear kinematic hardening laws for expressing the Bauschinger effect and the transient Bauschinger behavior. The distance between the bounding and yield surfaces is used to regulate the elastic modulus of a material during deformation. The bounding surface and yield surface equations are given below [17].

$$f = f_y\,(\sigma_{ij} - \alpha) - Y^2 \tag{22}$$

$$F = f_y\,(\sigma_{ij} - \beta) - (B + R)^2 \tag{23}$$

where f_y is a function that describes the form of the yield criterion, α is backstress, Y is yield stress, β is the center of the bounding surface, B is the initial size of the bounding surface, and R is the isotropic hardening component. The motion of back-stress is expressed as follows [32]:

$$\alpha = \alpha_* + \beta \tag{24}$$

where α_* is the relative motion of the yield surface and β is the center of the bounding surface. The evolution of α_* is given by [32].

$$\mathring{\alpha}_* = C\left[\left(\frac{a}{Y}\right)(\sigma_{ij} - \alpha) - \sqrt{\frac{a}{\bar{\alpha}_*}}\alpha_*\right]\dot{\bar{\varepsilon}}_p \tag{25}$$

where $\dot{\bar{\varepsilon}}_p$ is the effective plastic strain rate, $\bar{\alpha}_* = f_y(\alpha_*)$, and a=B+R-Y. The evolution of β is given by [32].

$$\mathring{\beta} = k\left(\frac{2}{3}bD^p - \beta\dot{\bar{\varepsilon}}_p\right) \tag{26}$$

where b and k are material parameters. The evolution of R is given by [32].

$$\dot{R} = k(R_{sat} - R)\dot{\bar{\varepsilon}}_p \tag{27}$$

where R_{sat} is the saturated value of isotropic hardening stress R at further plastic strain. Unlike forward loading, Yoshida and Uemori [17] found that the hardening rate decreased when the load was reversed; they called it workhardening stagnation. To capture this behavior, they introduced the non-IH surface as the condition for determining the evolution of the isotropic hardening component. The equation of non-IH surface according to the center of the bounding surface is given by [17].

$$g_\sigma = f_y(\beta - q) - r^2 \tag{28}$$

where q and r are the center and the radius of the non-IH surface. The kinetic motion of non-IH surface is defined as [32]

$$\begin{gathered} \dot{q} = \mu(\beta - q) \\ \mu = \frac{1 - h\Gamma\dot{r}}{r}\ ;\ \Gamma = \frac{(\beta - q):\dot{\beta}}{r} \end{gathered} \tag{29}$$

where h ($0 \le h \le 1$) is a material parameter that controls the rate of expansion of the non-IH surface. The evolution of r is given by[32].

$$\begin{gathered} \dot{r} = h\Gamma\ when\ \dot{R} > 0 \\ \dot{r} = 0\ when\ \dot{R} = 0 \end{gathered} \tag{30}$$

Finally, to describe the non-constant elastic modulus behavior of a material during deformation, Yoshida et al. [33] introduced the average elastic modulus instead of the constant elastic modulus, which is expressed by the following equation [33]:

$$E_{av} = E_0 - (E_0 - E_a)\left[1 - exp\left(\xi\varepsilon_p\right)\right] \tag{31}$$

where E_0 and E_a are the elastic modulus at the beginning and the elastic modulus at further plastic strain, and ξ is the material parameter. In summary, ten material parameters for the Y-U model can be received in two tests: a tension-compression test for seven parameters (C,

B, R_{sat}, Y, b, h, and m) and load-unload tensile testing for three parameters (E_0, E_a, and ξ).

3. Material Characterization and Forming Limit Diagram Determination

3.1. Uniaxial Tension Test

The commercial advanced high-strength steel sheet named NSC980D with an initial thickness of 1 mm was used in this study. A uniaxial tension test was performed on an Instron hydraulic universal testing machine with a constant crosshead speed of 0.48 mm/min, and the strain was measured by the digital image correction (DIC) technique. The tension specimen dimensions are according to ASTM E8 [34]. Since steel sheets are an anisotropic material, each loading direction can produce different properties. Therefore, the specimens were prepared at 0°, 45°, and 90° relative to the rolling direction (RD) to capture the behavior. The stress-strain response of NSC980D in three directions is shown in Fig. 1. The yield strength of NSC980D in three different directions was determined by the offset method at 0.2% strain. The Lankford coefficients, or r-values, at different angles were tested under ASTM E517 [35] and calculated using the volume constancy assumption based on the strain in the longitudinal and transverse directions of the specimen at 10% of total elongation. Additionally, the results of the mechanical properties of NSC980D, i.e., Young's modulus (E), yield stress (YS), ultimate tensile strength (UTS), total elongation (TE), and r-value —are presented in Table 1.

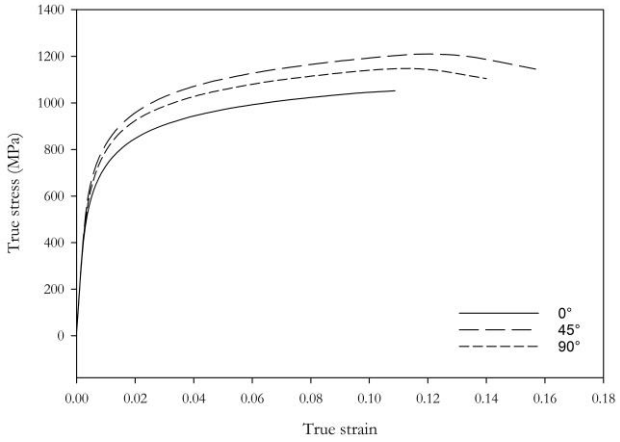

Fig. 1. Stress-strain response of NSC980D.

Table 1. Material properties of NSC980D. [36]

Dir	E (GPa)	YS (MPa)	UTS (MPa)	TE (%)	r-value
0°	189	656	936	9.04	0.82
45°	188	759	1066	10.1	0.83
90°	190	710	1032	10.04	0.92

3.2. Strain-Based Forming Limit Diagram

The Nakajima stretch test is an appropriate method for obtaining the experimental ε-FLD due to its uncomplicated tool setup, and the strain state results cover almost the range [27] of the ε-FLD for the stamping process. The Nakajima stretch test was performed on an Erichsen universal sheet metal testing machine according to ISO 12004-2 [37]. To create the various limits of the strain state, the specimen geometries were prepared following Panich et al. [5] using nine blank widths (W) ranging from 20mm to 190mm. The specimen geometry and dimensions are shown in Fig. 2. As a result, nine differences in strain state limits were produced. Wire-cut EDM was used to prepare the specimens, and an electrochemical technique was applied to create a circle grid diameter of 2.5mm on each specimen. A hemispherical punch with a diameter of 100mm was used to deform the specimens at a speed of 10mm/min until a fracture appeared, as demonstrated in Fig. 3. The deformed circle grid around the fracture zone was chosen to determine strain, and then the DIC technique was used to measure the major and minor strains. The relationships between major and minor strains for the nine different specimen geometries are summarized in Fig. 4.

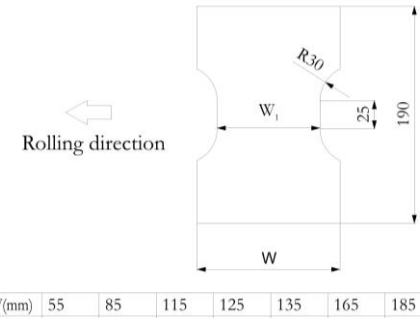

W(mm)	55	85	115	125	135	165	185	195	190
W_1(mm)	20	50	80	90	100	130	150	160	190

Fig. 2. Geometry and dimension of specimens in the Nakajima stretch test.

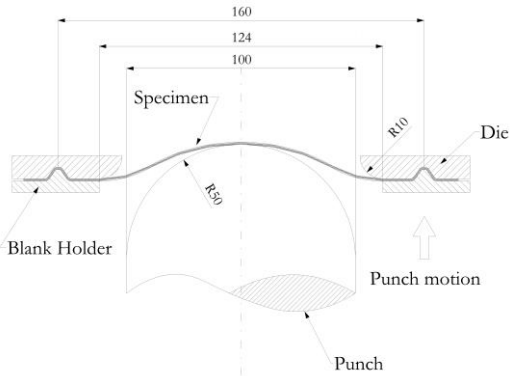

Fig. 3. Schematic of Nakajima testing setup.

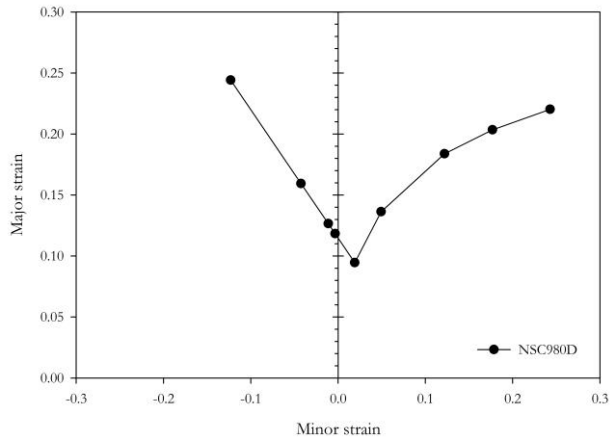

Fig. 4. The determined ε-FLD from the Nakajima stretch test. [36]

3.3. Tension and Compression Test

To achieve a good sheet metal forming prediction, a material model should closely represent the material's actual response. The advantage of kinematic hardening over isotropic hardening is its ability to explain the Bauschinger effect when the metal is reverse loaded. This scenario occurs when sheet metal is drawn into a draw bead or die radius. The kinematic hardening parameter can be obtained from the tension and compression tests. This test was performed on an Instron hydraulic universal testing machine with a modified specimen based on the standard SEP1240 [38], with strain measured using the DIC technique.

First, the specimens shown in Fig. 5 were clamped by a spring-loaded fixture, similar to the method used by Julsri et al. [16] to prevent buckling during the compression stage. The specimens were then held at both ends by a crosshead gripper and stretched at a constant crosshead speed of 1 mm/min until the strain reached approximately 10%. Afterward, the load direction was reversed to apply a compressive load until the stress reached a steady state. The stress-strain response of the tension and compression test is illustrated in Fig. 6.

The Y-U model parameters can be identified by separating the tension-compression curve into forward and reversal stages. The forward stage can be represented by the Voce hardening equation, where the parameters Y, B, (Rsat + b), and k are derived from this stage. The parameters b and C are associated with the reversal stage, and h is an adjustment parameter used to correct the tension-compression curve to match the experimental results, which can be identified through numerical simulation. The function parameters of the Y-U model are summarized in Table 2. The parameters for the average elastic modulus function from Eq. (31) are given in Table 3.

Unlike the Y-U, the isotropic hardening laws require only forward loading to determine the function parameter. For the Swift hardening model, three parameters following Eq. (21) express the strain-hardening behavior. The determined Swift hardening model parameters are tabulated in Table 4. Figure 6 illustrates the different types of hardening models in strain-hardening prediction. Without accounting for the Bauschinger effect, isotropic hardening laws, like the Swift hardening model, tend to overpredict in the reversal state.

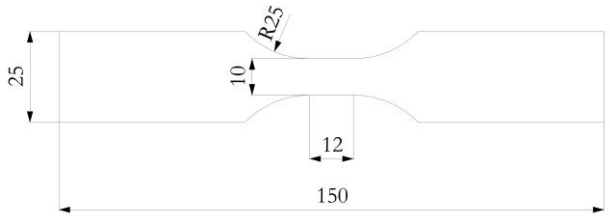

Fig. 5. Geometry and dimension of specimen in tension and compression test.

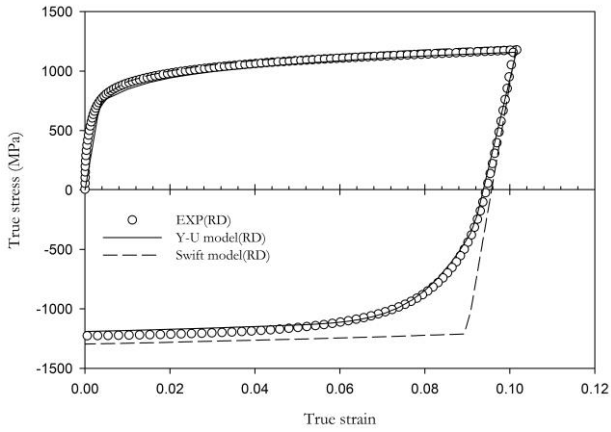

Fig. 6. Comparison of NSC980D's stress-strain behavior under the RD condition between predictions from hardening models and actual results from tension and compression tests.

Table 2. The material parameters of the Y-U model for NSC980D under the RD condition.

Y (MPa)	B (MPa)	R_{sat} (MPa)	b (MPa)	C	k	h
733	927.89	267.96	58.94	132.13	14.09	0.5

Table 3. The average elastic modulus function parameter for NSC980D under the RD condition. [16]

E_0 (GPa)	E_{sat} (GPa)	ξ
208.91	128.40	14.19

Table 4. The Swift hardening model function parameters for NSC980D under the RD condition.

K (GPa)	ε_0	n
1496	0.001066	0.1052

DOI:10.4186/ej.2024.28.9.51

3.4. Determination of Anisotropy Coefficients for Different Yield Functions

The anisotropy coefficients for Hill48 and Barlat89 can be calculated using Eq. (4) and Eq. (8) with the r-value in three directions (r_0, r_{45}, and r_{90}). For Yld2000, eight mechanical parameters are required to determine the Yld2000 anisotropy coefficients, which consist of yield stress and r-value in three uniaxial directions and a balanced biaxial condition. Because of this research, the necessary testing equipment is absent in the balanced biaxial condition. Therefore, the yield stress in the balance biaxial was assumed to be equal to two different conditions: first, equal to the rolling direction: $\sigma_b=\sigma_0$, and second, equal to the average yield stress in 0°, 45°, and 90° to RD: $\sigma_b=\sigma_{av}=(\sigma_0+2\sigma_{45}+\sigma_{90})/4$. The r-value in the balanced biaxial condition was calculated using the Yld96 yield function under the assumption of a BCC crystal structure.

The calculation methodology of anisotropy coefficients for Yld96 and Yld2000 are provided in Appendix A and B. The results of the anisotropy coefficient determinations for different yield criteria are summarized separately in Tables 5–8. It should be noted that when mechanical properties are only a difference in the σ_b value, the anisotropy coefficients of Yld96 will vary only slightly. Figure 7 shows the normalized yield stress, r-value, and yield surface predicted by different yield criteria compared to the experiment result. Observable deviations from the experimental results occurred when Hill48 and Barlat89 predicted the yield stress in different directions from RD because they did not account for the behavior of yield stress in the determination of the yield function coefficients.

Table 5. Anisotropy coefficients of Hill48(r-value).

F	G	H	N
0.9794	1.0988	0.9010	2.7642

Table 6. Anisotropy coefficients of Barlat89(r-value).

A	C	H	P	m
1.0676	0.924	0.9592	0.9639	6

Table 7. Anisotropy coefficients of Yld96 under different yield stresses in biaxial condition.

Anisotropy coefficients	$\sigma_b=\sigma_0$	$\sigma_b=\sigma_{av}$
c_1	0.90238	0.90236
c_2	0.94620	0.94620
c_3	0.99486	0.99486
c_6	0.95644	0.95643
α_x	1.81460	1.81460
α_y	1.41200	1.41200
α_{z0}	1.00000	1.00000
α_{z1}	1.16200	1.16200

Table 8. Anisotropy coefficients of Yld2000.

Anisotropy coefficients	$\sigma_b=\sigma_0$ $r_b=1.1422$	$\sigma_b=\sigma_{av}$ $r_b=1.1423$
α_1	1.0260	0.9768
α_2	0.8843	0.8819
α_3	1.1641	0.9494
α_4	0.9797	0.9376
α_5	0.9852	0.9571
α_6	0.8738	0.6997
α_7	0.8736	0.8574
α_8	0.7121	0.8343

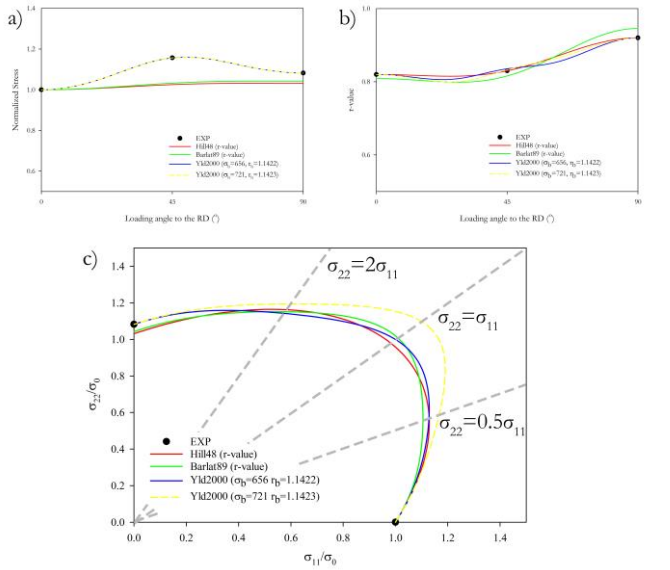

Fig. 7. Comparisons of experimental and prediction results that were calculated from difference yield criteria. (a) r-values in variation angle to the RD. (b) yield stresses in variation angle to the RD. (c) yield surface contours.

3.5. Determining Stress-Based Forming Limit Diagrams

The σ-FLD represents the forming limit boundary for workpieces during the forming process, utilizing the relationship between major and minor stresses rather than major and minor strains, as seen in the ε-FLD. In this study, the σ-FLD was determined based on experimental results from the ε-FLD using a finite element simulation of Nakajima stretch forming conducted with commercial finite element software named PAM-STAMP. The simulation setup for the Nakajima stretch test was replicated based on the ε-FLD determination setup from the previous section, including the die set and specimens. The specimen and simulation setup are illustrated in Figs. 2, 3 and 8. The die set was modeled using rigid shell elements, while the specimens were constructed using BELYTSCHKO-TSAY shell elements. To reduce computation time, the specimen in the simulation was scaled to one-fourth of its original size. Coulomb friction coefficients were set at 0.05

between the punch and specimen to reduce the stress effects caused by friction, and at 0.12 between the blank holder and die to maintain the grip ability of the specimen. Three yield functions—Hill48, Barlat89, and Yld2000—coupled with hardening laws—Swift and Y-U—were employed to describe the specimen's behavior during deformation. The ε-FLD determined from the experiment in the prior section was used as a failure criterion. Elements that reached the strain-based forming limit curve were selected to examine the major and minor stresses. The stress-based forming limit curves derived from the different yield functions coupled with hardening models are summarized in Fig. 9.

The variation in yield criteria and hardening models on σ-FLD determination resulted in differences in the shape of the σ-FLD and the amount of stress variation developed in the major stress direction. However, the major stress interception point does not occur in the uniaxial state compared to the work by Panich [39] and Jantarasricha et al. [40] due to differences in the methodology for determining the σ-FLD. The theoretical calculations by Panich [39] and Jantarasricha et al. [40] are unaffected by friction. In contrast, friction cannot be eliminated in the Nakajima stretch simulation, resulting in the development of minor stress.

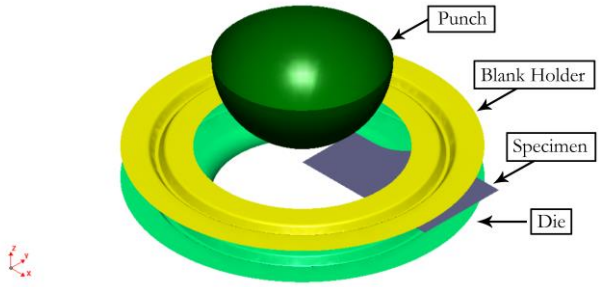

Fig. 8. Nakajima stretch test modeled in PAM-STAMP.

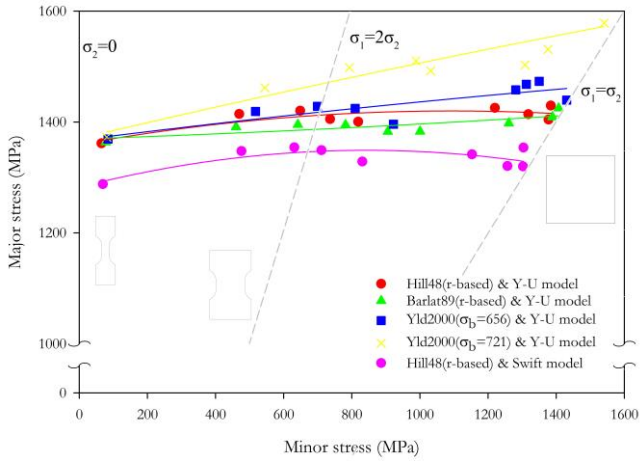

Fig. 9. Comparison of σ-FLD generated from different yield criteria and hardening models.

4. Result and Discussion

4.1. Crack Prediction Ability of Strain and Stress Based Forming Limit Diagram

To investigate the failure prediction capability of the ε-FLD and σ-FLD, experimental stamping tests of an automotive roof frame component named Panel-RF FRT HRD were carried out. The experiment was performed on a mechanical eccentric press machine. The upper surface is the die that connects to the ram, while the lower surfaces consist of the punch and blank holder, which are connected to the press table and cushion system, respectively. During the test, a blank holding force of 9 tons was used to prevent the forming part from wrinkling. The forming process was successful without visible fractures in the assembled area, as seen in Fig. 10. It should be noted that the fracture at the bottom left and right of the workpiece will be trimmed out later. However, the area near the outer punch radius exhibited a small crack, as seen in Fig. 11. The crack is 25mm long along the length of the workpiece, and its distance from the center of the workpiece was 88 mm.

Subsequently, finite element simulations of the Panel-RF FRT HRD were performed to investigate the crack area. The simulation was set to a single-action press mode. All the die set faces used in this simulation were imported from the CAD file received from the manufacturer of the Panel-RF FRT HRD. The simulation was set up as Fig. 12; the tooling was created by shell elements and was defined as a rigid body. The initial blank size is 225x1000x1 mm in width, length, and thickness, respectively. The mesh size was set to the validation strategy as recommended by the software [41]; as a result, the initial element size was 14 mm, and the four refinement levels resulted in the smallest possible element size being 0.875 mm. The friction coefficient on the tooling surface was set to 0.12 as suggested by the software. The total drawing depth is 26 mm. Different sets of yield criteria and hardening models are used to describe the material's behavior during forming. This simulation uses ε-FLD and σ-FLD from the previous section as the failure criteria. The simulation results indicated that the crack initiated and stopped growth at 3.8mm and 2.6mm before the die completely traveled to the end position. The two green lines in Fig. 13 indicate the initiation and end of the crack. Line number 1 indicates the end of the crack, and line number 2 indicates the initiation point. Both lines are away from the center of Panel-RF FRT HRD at 108mm and 83mm, respectively. The capability of s-FLD and e-FLD in crack prediction will be discussed in two parts.

1. Capability of ε-FLD in crack prediction: Fig. 13 indicates an underestimate in the crack length prediction, with a predicted crack length of 21.5 mm instead of the actual 25 mm. A similar situation occurred with Barlat89 & Y-U and Yld2000 (σ_b=721) & Y-U. However, when using Yld2000 (σ_b = 656) with the Y-U model, and

Hill48 with the Swift model to represent the material's properties, the predicted crack length corresponded well with the actual measurements. The strain history of the white color element in Fig. 13 is selected to provide an overview of the strain history across different combinations of yield criteria and hardening models. as summarized in Fig. 14. All the strain histories in Figure 14 show a slight path change from the beginning and finish near the plane strain state. This circumstance is reasonable to the actual formed Panel-RF FRT HRD because the crack area is in the bending area. However, the path of the strain histories in Fig. 14 is different. This situation exists because each yield criterion generates a distinct material's behavior response, as is visible on the yield surface in Fig. 7©. The smallest size of the yield surface under the plane strain state with a major load in TD ($\sigma_{22}=2\sigma_{11}$ line) that Yld2000(σ_b=656) generated indicates the fastest yielding in this state. This results in high strain development, which causes the strain history of Yld2000(σ_b=656) to show the highest major strain. Unfortunately, the cause of the higher strain developed in the Swift model than in the Y-U model is not clear in this part. However, the authors believe that this is due to strain hardening, as each hardening model has its unique approach to developing strain hardening during forming simulation.

2. Capability of σ-FLD in crack prediction: Figure 15 shows that the predicted crack lengths by all material models closely matched the actual measurements. The stress history of the white color element in Fig. 15, which is the same element shown in Fig. 13, is selected to provide an overview of the stress history across different combinations of yield criteria and hardening models, as summarized in Fig. 16. A noticeable aspect of Fig. 16 is the clear presentation of the development progress of the white element at the beginning. Additionally, the stress history reveals a slight change during deformation, illustrated by a wavy line that is difficult to visualize on the strain history. Overall, failure prediction by σ-FLD is better than by ε-FLD because all the stress histories reached the σ-FLC without concern for the material model. Although all the material models used in this research successfully predicted failure under stress assumptions, the assumed σb value for Yld2000 without experiment should be avoided because an assumed σ_b value affects the yield surface from the early plane state until the equi-biaxial state as seen in Fig. 7(c), which can decrease the accuracy of prediction, especially when plane strain is concerned.

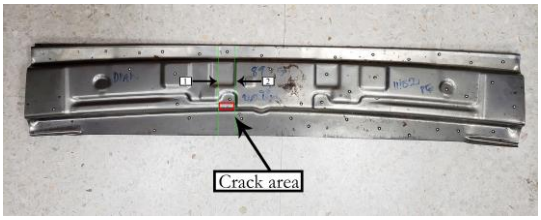

Fig. 10. The already formed Panel-RF FRT HRD.

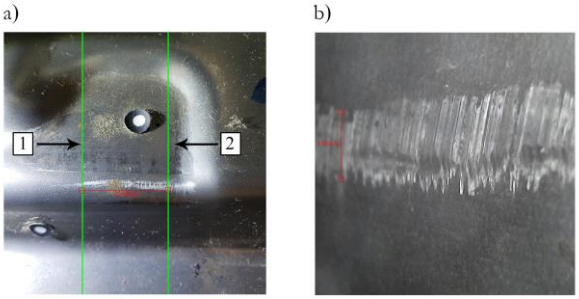

Fig. 11. A close-up view of the crack area (a) The length of the crack (b) The width of the marking lines.

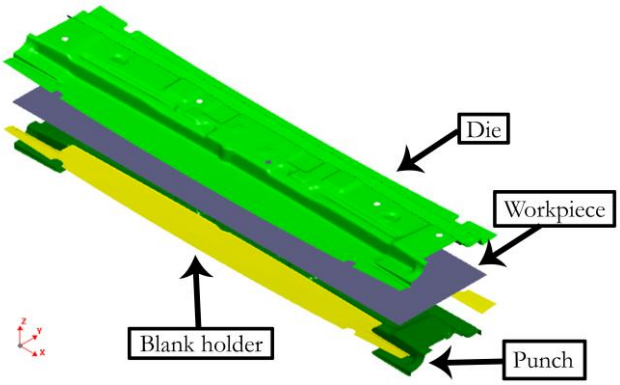

Fig. 12. Simulation setup of part Panel-RF FRT HRD.

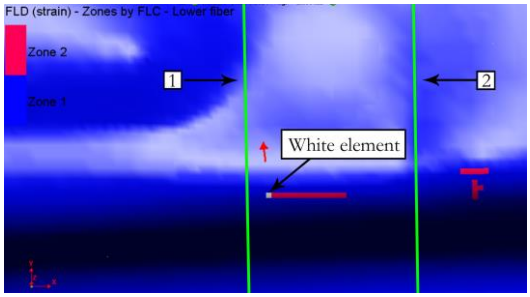

Fig. 13. The crack (shown in magenta) predicted by ε-FLD under Hill48&Y-U material's properties expression.

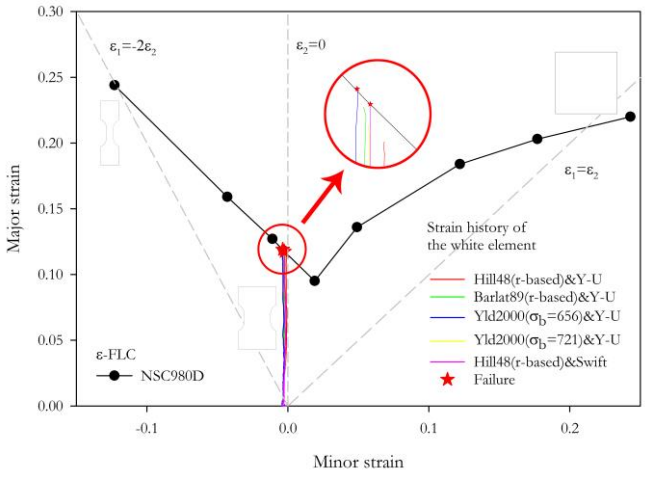

Fig. 14. The strain history of the white element is calculated by different yield criteria and hardening models.

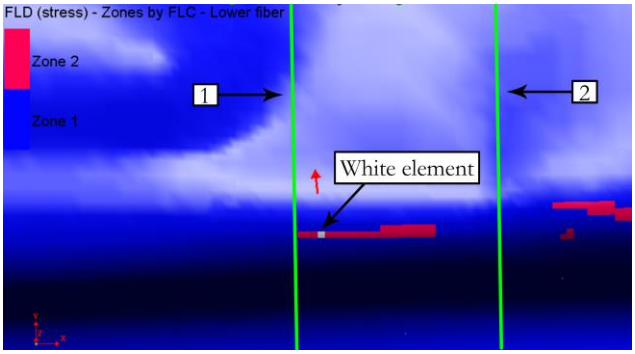

Fig. 15. The crack (shown in magenta) predicted by σ-FLD under Hill48&Y-U material's properties expression.

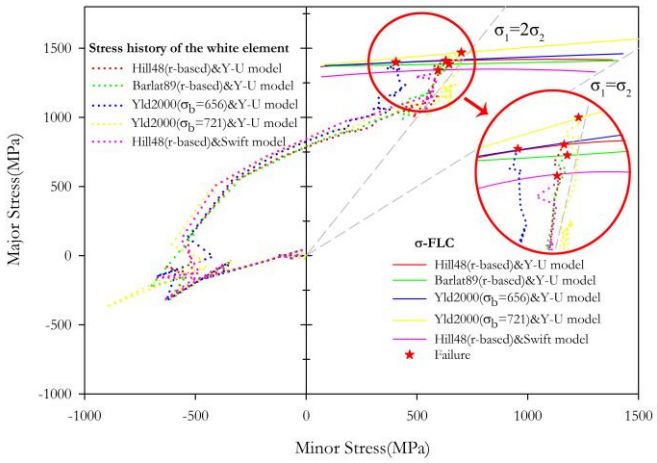

Fig. 16. The strain history of the white element is calculated by different yield criteria and hardening models.

4.2. Springback Prediction

To analyze the effects of different yield criteria and hardening models on springback prediction, the springback simulation was conducted in PAM-STAMP under an implicit solver. After the springback computation is successful, a 3D scan of the stamped part Panel-RF FRT HRD is used to estimate the validity of the simulation result. The validation of springback prediction in this study uses the area enclosed between two curves of section view from a 3D scan of a real stamped workpiece and a simulation; the greater the area enclosed, the less accurate the prediction. This method is used instead of angle measurement due to the variety of curvature in this workpiece, which makes it difficult to define a datum. The area between the two curves was measured on Siemens NX software, as shown in Fig. 17. Three cross-sections were used to validate the springback prediction results, located 150 mm, 500 mm, and 760 mm away from the left side of the workpiece to the right. The positions of the three cross-sections are illustrated in Fig. 18. The areas enclosed between the cross-section curve from the 3D scan and the simulation results for the different yield criteria and hardening models in Figs. 19-21 are summarized in Table 9.

Hill48, coupled with the Y-U model, provided the best springback prediction result in this comparison, followed by Barlat89 integrated with the Y-U model, Yld2000 (σ_b = 656) integrated with the Y-U model, Yld2000 (σ_b = 721) integrated with Y-U model, with the least accurate springback prediction found with Hill48 coupled with the Swift model. According to the experiment results, the hardening model plays a more important role than the yield criteria in springback prediction, as evident when varying hardening models within the same yield criteria. Undoubtedly, the Y-U model offers superior predictive ability compared to the Swift model, as evidenced by the hardening behavior shown in Fi. 6, which more closely aligns with the results from tension-compression tests. Additionally, the springback prediction results indicate that Yld2000 provides less accuracy than Hill48 under the same hardening model conditions, which is inconsistent with the findings of Uemori et al. [15]. The issue arises because both assumed σ_b values generate an improper yield surface curvature between the plane strain state and the equi-biaxial state, as shown in Fig. 7(c), along with Panel-RF FRT HRD, which contains multiple bending areas along RD, as depicted in Figs. 19-21, associated with a plane strain state in TD. This reason makes Yld2000 less accurate for springback predictions in this experiment.

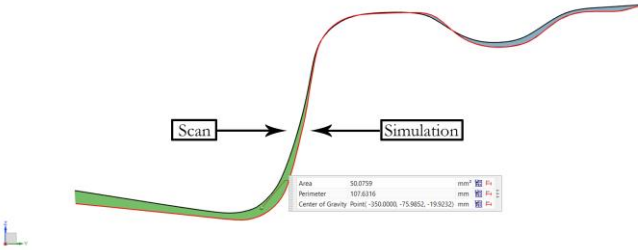

Fig. 17 The measurement area is enclosed between the 3D scan and the Hill48&Y-U profile in Section A by Siemens NX.

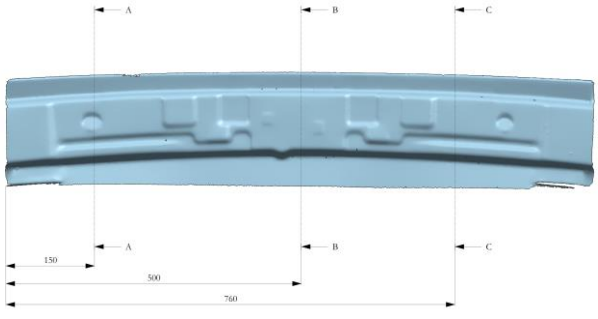

Fig. 18 The cross-section position is illustrated in the 3D scan of Panel-RF FRT HRD.

DOI:10.4186/ej.2024.28.9.51

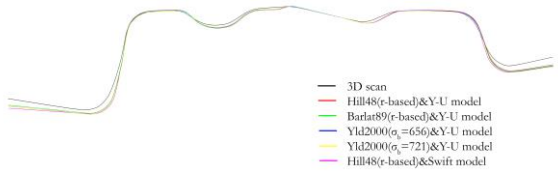

Fig. 19. The comparison of cross-section profile in section A.

Fig. 20. The comparison of cross-section profile in section B.

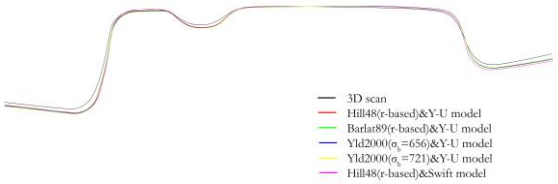

Fig. 21. The comparison of cross-section profile in section C.

Table 9. The area enclosed between 3D scan and simulation cross-section profile.

Yield function &Hardening model	Section A (mm^2)	Section B (mm^2)	Section C (mm^2)	Total (mm^2)
Hill48 &Y-U model	112.42	89.43	105.20	307.05
Barlat89 &Y-U model	115.32	85.83	111.02	312.16
Yld2000(σ_b=656) &Y-U model	130.69	81.66	126.48	338.83
Yld2000(σ_b=721) &Y-U model	135.09	83.87	120.44	339.41
Hill48 &Swift model	136.98	118.90	118.01	373.88

4.3. Thickness Prediction

To examine the effects of different yield criteria and hardening models on thickness prediction in the simulation process, thickness measurements were taken at various locations on the actual stamped workpiece, which initially had a thickness of 1 mm. These measurements were performed using a digital micrometer with ball anvil-spindle tips, as shown in Fig. 22, and then compared with the simulation results. Figure 23 shows the four sample points were used in this study. The first and second points are located on the left and right sides of the workpiece, which is the largest thinning predicted by PAM-STAMP. The third and fourth positions are located near the middle of the workpiece length. The different measurement sample locations represent the different states of strain: the first and second positions represent biaxial tension, while the third and fourth positions represent plane strain and uniaxial compression. The thickness measurements at different locations for the actual formed workpiece and the simulation are summarized in Table 10. The mean absolute percentage error (MAPE) is used to measure the accuracy of each prediction condition. The MAPE equation is given in Appendix C.

The result shows that Hill48 coupled with the Y-U model provides the best thickness prediction result in this comparison, followed by Barlat89 integrated with the Y-U model, Yld2000 (σ_b = 656) integrated with the Y-U model, Yld2000 (σ_b = 721) integrated with the Y-U model, and finally, the least accurate thickness prediction was found with Hill48 coupled with the Swift model. The thickness comparison in Table 10 indicated that the hardening model had a more significant influence on the thickness prediction than the yield criteria. This case is due to the slight differences between yield surfaces. However, Güner et al. [42] found that the Yld2000 is generally better at predicting thickness than Hill48, which conflicts with this research. This disagreement is because Yld2000 in this research lacks σ_b and r_b from experiments. This finding also shows that σ_b and r_b are crucial for Yld2000 to improve its prediction ability. A similar situation occurred with the BBC2005 yield function in the absence of σ_b, which was found in Banabic and Sester's [43] work. The last point is the influence of the hardening model on thickness prediction results. Although Fig. 6 shows that the Swift and Y-U models have similar forward loading, there is a significant difference in the thickness prediction for Panel-RF FRT HRD. This discrepancy can be explained in two topics: First, the number of loading directions. Figure 6 considers loading in only one direction, while stamping involves multiple directions. Second is the hardening model theory. The Swift model only expands a yield surface, whereas the Y-U can expand the yield surface and translate its center. Thus, the Swift model results in equal stress development in both loading directions, while the Y-U model leads to unequal stress development in the two directions. For this reason, the Y-U model provides better results in thickness prediction.

Fig. 22. The thickness measuring tool is measuring at sample point 1.

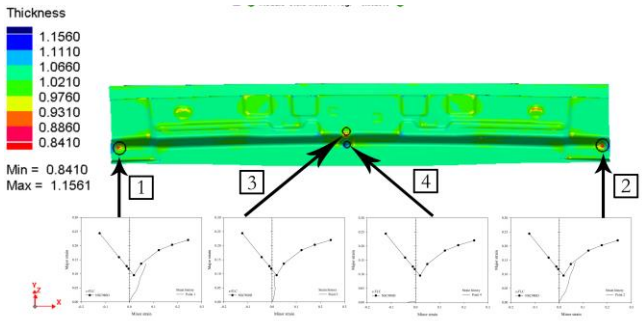

Fig. 23. Four measurement positions and their relation to strain histories.

Table 10. The thickness comparison between the actual experiment and different simulation conditions.

Yield function & hardening model	Point 1 (mm)	Point 2 (mm)	Point 3 (mm)	Point 4 (mm)	MAPE (%)
Experiment	0.850	0.862	0.945	1.068	-
Hill48 &Y-U	0.849	0.844	0.924	1.075	1.249
Barlat89 &Y-U	0.839	0.837	0.913	1.074	2.031
Yld2000 (σ_b=656) &Y-U	0.844	0.843	0.896	1.087	2.436
Yld2000 (σ_b=721) &Y-U	0.853	0.845	0.876	1.076	2.613
Hill48 &Swift	0.833	0.833	0.881	1.076	3.193

5. Conclusion

The σ-FLD was constructed by a simulation of the Nakajima stretch in PAM-STAMP software. The yield criteria and hardening models are used to express material's behavior during deformation, and the experiment ε-FLD is used for the simulation termination criterion. Since the yield criterion and hardening law are the important variables in this σ-FLD construction method, the influence of yield criteria and hardening models on the springback and thickness prediction was also studied. The result can be summarized as follows:

1. All the constructed σ-FLD from the ε-FLD show better crack prediction than the ε-FLD for every combination of yield criteria and hardening models.

2. The variation in σ-FLC response when using the different combinations of yield criteria and hardening models indicated the σ-FLD is highly influenced by yield criteria and hardening models. Therefore, the σ-FLD determined by this method should be precise in failure prediction when a simulation is done using the same combination of yield criteria and hardening model.

3. Hill48 integrated with the Y-U model performed the best for both spring back and thickness prediction, followed by the Y-U model integrated with Barlat89, Yld2000(σ_b=656), and Yld2000(σ_b =721). The worst springback and thickness prediction accuracy in this study was found on Hill48 integrated with the Swift model.

4. The Y-U model improves both springback and thickness prediction under the same yield function.

5. The Yld2000 with six mechanical parameters did not improve precision in either springback or thickness prediction in this study.

Acknowledgement

The authors would like to thank King Mongkut's University of Technology Thonburi (KMUTT) for the Petchra Pra Jom Klao Master's Degree Research Scholarship, as well as Thai Summit Automotive Co., Ltd. for the material support and sample of automotive parts.

Appendix A. Calculation of anisotropy coefficients for the Yld96 yield function

To determine the seven anisotropy coefficients: parameters c_1, c_2, c_3, c_6, a_x, a_y, and a_{z1}. The seven equations are used and then solved by the Newton-Raphson method. The sequence of solving the function parameter is Eqs. (A1) to (A4) for c_1, c_2, c_3, and c_6, followed by Eqs. (A5) to (A7) for a_x, a_y, and a_{z1}. If the r-value is not satisfied, then recalculate Eqs. (A1) to (A4) and Eqs. (A5) to (A7) again until satisfied with the calculation result of the r-value. The seven equations are expressed as follows [44, 45]:

$$F_1 = \alpha_x|c_2 - c_3|^m + \alpha_y|2c_2 + c_3|^m + \alpha_{z0}|c_2 - 2c_3|^m - 2\left(\frac{3\bar{\sigma}}{\sigma_0}\right)^m = 0 \quad \text{(A1)}$$

where $\bar{\sigma}(\sigma_{xx}=\sigma_0, \sigma_{yy}=0, \sigma_{xy}=0)$-$\sigma_0$=0

$$F_2 = \alpha_x|2c_1 + c_3|^m + \alpha_y|c_3 - c_1|^m + \alpha_{z0}|2c_3 + c_1|^m - 2\left(\frac{3\bar{\sigma}}{\sigma_{90}}\right)^m = 0 \quad \text{(A2)}$$

where $\bar{\sigma}(\sigma_{xx}=0, \sigma_{yy}=\sigma_{90}, \sigma_{xy}=0)$-$\sigma_{90}$=0

$$F_3 = \alpha_x|2c_1 + c_2|^m + \alpha_y|2c_2 + c_1|^M + \alpha_{z0}|c_2 - c_1|^m - 2\left(\frac{3\bar{\sigma}}{\sigma_b}\right)^m = 0 \quad \text{(A3)}$$

where $\bar{\sigma}(\sigma_{xx}=\sigma_b, \sigma_{yy}=\sigma_b, \sigma_{xy}=0)$-$\sigma_b$=0

$$F_4 = \alpha_1\left|(c_1+c_2)-\sqrt{\left(\frac{c_2-c_1}{3}\right)^2+(2c_6)^2}\right|^m + \alpha_2\left|(c_1+c_2)+\sqrt{\left(\frac{c_2-c_1}{3}\right)^2+(2c_6)^2}\right|^m + \alpha_3\left|2\sqrt{\left(\frac{c_2-c_1}{3}\right)^2+(2c_6)^2}\right|^m - 2\left(\frac{4\bar{\sigma}}{\sigma_{45}}\right)^m = 0 \quad \text{(A4)}$$

where $\bar{\sigma}(\sigma_{xx}=\sigma_{45}/2, \sigma_{yy}=\sigma_{45}/2, \sigma_{xy}=\sigma_{45}/2)-\sigma_{45}=0$ For α_x, α_y, and α_{z1} can be calculated iteratively from the following equation [44]:

$$F_5 = (r_0)_{theory} = \frac{\bar{\sigma}}{\left(\frac{\partial\bar{\sigma}}{\partial\sigma_x}+\frac{\partial\bar{\sigma}}{\partial\sigma_y}\right)\sigma_0} - 1 - r_0 = 0 \quad \text{(A5}$$

where $\bar{\sigma}(\sigma_{xx}=\sigma_0, \sigma_{yy}=0, \sigma_{xy}=0)-\sigma_0=0$

$$F_6 = (r_{90})_{theory} = \frac{\bar{\sigma}}{\left(\frac{\partial\bar{\sigma}}{\partial\sigma_x}+\frac{\partial\bar{\sigma}}{\partial\sigma_y}\right)\sigma_{90}} - 1 - r_{90} = 0 \quad \text{(A6)}$$

where $\bar{\sigma}(\sigma_{xx}=0, \sigma_{yy}=\sigma_{90}, \sigma_{xy}=0)-\sigma_{90}=0$

$$F_7 = (r_{45})_{theory} = \frac{\bar{\sigma}}{\left(\frac{\partial\bar{\sigma}}{\partial\sigma_x}+\frac{\partial\bar{\sigma}}{\partial\sigma_y}\right)\sigma_{45}} - 1 - r_{45} = 0 \quad \text{(A7)}$$

where $\bar{\sigma}(\sigma_{xx}=\sigma_{45}/2, \sigma_{yy}=\sigma_{45}/2, \sigma_{xy}=\sigma_{45}/2)-\sigma_{45}=0$

Appendix B. Calculation of anisotropy coefficients for the Yld2000 yield function

To determine the eight anisotropy coefficients: $\alpha_1, \alpha_2, \alpha_3, \alpha_4, \alpha_5, \alpha_6, \alpha_7$, and α_8, the eight equations (Eqs. (B1) to (B4)) from [21, 46] are used, then solved by the Newton-Raphson method for the eight equations simultaneously. The eight equations are expressed as follows:

For α_1 to α_6

$$F_i = |\alpha_1\gamma_i - \alpha_2\delta_i|^m + |\alpha_3\gamma_i - 2\alpha_4\delta_i|^m + |2\alpha_5\gamma_i - \alpha_6\delta_i|^M - 2\left(\frac{\bar{\sigma}}{\sigma_i}\right)^m = 0 \quad \text{(B1)}$$

$$g_i = (\alpha_1 q_{xi} + \alpha_2 q_{yi})(\alpha_1\gamma_i - \alpha_2\delta_i)|\alpha_1\gamma_i - \alpha_2\delta_i|^{m-2} + (\alpha_3 q_{xi} - 2\alpha_4 q_{yi})(\alpha_3\gamma_i + 2\alpha_4\delta_i)|\alpha_3\gamma_i + 2\alpha_4\delta_i|^{m-2} + (2\alpha_5 q_{xi} - \alpha_6 q_{yi})(2\alpha_5\gamma_i + \alpha_6\delta_i)|2\alpha_5\gamma_i + \alpha_6\delta_i|^{m-2} = 0 \quad \text{(B2)}$$

where i = 1, 2, 3. The values of γ_i, δ_i, q_{xi} and q_{yi} are noted in Table11.

For α_7 to α_8

$$F_4 = \left|\frac{\sqrt{U_2'^2+4\alpha_7^2}}{2}\right|^m + \left|\frac{3U_1''-\sqrt{U_2''^2+4\alpha_8^2}}{4}\right|^m + \left|\frac{3U_1''+\sqrt{U_2''^2+4\alpha_8^2}}{4}\right|^m - 2\left(\frac{\bar{\sigma}}{\sigma_{45}}\right)^m = 0 \quad \text{(B3)}$$

$$g_4 = V_1\frac{U_2'^2}{\sqrt{U_2'^2+4\alpha_7^2}} + \frac{3}{2}U_1''(V_2+W) + \frac{1}{2}\frac{U_2''^2}{\sqrt{U_2''^2+4\alpha_8^2}}(W-V_2) - \frac{2m\bar{\sigma}^m}{\sigma_{45}(1+r_{45})} = 0 \quad \text{(B4)}$$

where

$$U_2' = \frac{\alpha_1-\alpha_2}{3} \quad \text{(B5)}$$

$$U_2'' = \frac{2\alpha_5+\alpha_6-2\alpha_3-2\alpha_4}{3} \quad \text{(B6)}$$

$$U_1'' = \frac{\alpha_3+2\alpha_4+2\alpha_5+\alpha_6}{9} \quad \text{(B7)}$$

$$V_1 = m\left(\frac{\sqrt{U_2'^2+4\alpha_7^2}}{2}\right)^{m-1} \quad \text{(B8)}$$

$$V_2 = m\left(\frac{3U_1''-\sqrt{U_2''^2+4\alpha_8^2}}{4}\right)\left|\frac{3U_1''-\sqrt{U_2''^2+4\alpha_8^2}}{4}\right|^{m-2} \quad \text{(B9)}$$

$$W = m\left(\frac{3U_1''+\sqrt{U_2''^2+4\alpha_8^2}}{4}\right)\left|\frac{3U_1''+\sqrt{U_2''^2+4\alpha_8^2}}{4}\right|^{m-2} \quad \text{(B10)}$$

Table 11. The parameters value for Eq. (B1) and Eq. (B2). [21]

Index, i	γ_i	δ_i	q_{xi}	q_{yi}
i = 1 (RD)	2/3	-1/3	1-r_0	2+r_0
i = 2 (TD)	-1/3	2/3	2+r_{90}	1-r_{90}
i = 3 (Balance biaxial)	-1/3	-1/3	1+2r_b	2+r_b

Appendix C. Calculation of mean absolute percentage error

The equation of MAPE is defined as:

$$MAPE = \frac{1}{N}\sum_{i=1}^{N}\left|\frac{A_i-P_i}{A_i}\right| \quad \text{(C1)}$$

where N is the number of total sample points, A and P are the actual thickness and predicted at the interested point.

References

[1] D. Banabic, "Formability of Sheet Metals," in *Sheet Metal Forming Processes: Constitutive Modelling and Numerical Simulation*, 1st ed. Springer Berlin Heidelberg, 2010, ch. 3, sec. 3.3, pp. 152-175.

[2] V. Uthaisangsuk, U. Prahl, and W. Bleck, "Stress based failure criterion for formability characterisation of metastable steels," *Comput Mater Sci,* Article vol. 39, no. 1 pp. 43-48, 2007.

[3] R. Arrieux, M. Boivin, and F. Le Maître, "Determination of the forming limit stress curve for anisotropic sheets," *CIRP Ann Manuf Technol,* vol. 36, no. 1, pp. 195-198, 1987.

[4] M. C. Butuc, J. J. Gracio, and A. Barata Da Rocha, "An experimental and theoretical analysis on the application of stress-based forming limit criterion," *Int. J. Mech. Sci.,* Article vol. 48, no. 4, pp. 414-429, 2006.

[5] S. Panich, F. Barlat, V. Uthaisangsuk, S. Suranuntchai, and S. Jirathearanat, "Experimental and theoretical formability analysis using strain and stress based forming limit diagram for advanced high strength steels," *Mater Des,* Article vol. 51, pp. 756-766, 2013.

[6] A. Nakwattanaset, S. Panich, and S. Suranuntchai, "Formability prediction of high-strength steel sheet using experimental, analytical and theoretical analysis based on strain and stress forming limit curves and its application to automotive forming parts," *Materwiss Werksttech,* vol. 54, no. 9, pp. 1122-1137, 2023.

[7] T. Altan and A. E. Tekkaya, "Plastic deformation-state of stress. yield criteria flow rule. and hardening rules," in *Sheet Metal Forming: Fundamentals*, 1st ed. ASM International, 2012, ch. 5, sec. 5.13, p. 66.

[8] S. Toros, A. Polat, and F. Ozturk, "Formability and springback characterization of TRIP800 advanced high strength steel," *Mater Des,* Article vol. 41, pp. 298-305, 2012.

[9] S. Panich, V. Uthaisangsuk, S. Suranuntchai, and S. Jirathearanat, "Investigation of anisotropic plastic deformation of advanced high strength steel," *Mater. Sci. Eng. A.,* vol. 592, pp. 207-220, 2014.

[10] F. Ozturk, S. Toros, and S. Kilic, "Effects of anisotropic yield functions on prediction of forming limit diagrams of DP600 advanced high strength steel," *Procedia Engineering,* vol. 81, pp. 760-765, 2014.

[11] S. Kilic, F. Ozturk, and S. Toros, "Analysis of Yield Criteria and Flow Curves on FLC for TWIP900 Steel," *EXP Tech,* vol. 44, no. 5, pp. 597-612, 2020.

[12] B. Wang, Y. Chang, S. Zang, X. Li, S. Yu, and C. Wang, "Effect of complicated deformation behaviors during cold stamping on springback prediction of DP980 steel," *Int J Adv Manuf Technol,* Article vol. 126, no. 11-12, pp. 4997-5015, 2023.

[13] A. Ghaei, D. E. Green, and A. Taherizadeh, "Semi-implicit numerical integration of Yoshida-Uemori two-surface plasticity model," *Int. J. Mech. Sci.,* Article vol. 52, no. 4, pp. 531-540, 2010.

[14] B. Chongthairungruang, V. Uthaisangsuk, S. Suranuntchai, and S. Jirathearanat, "Springback prediction in sheet metal forming of high strength steels," *Mater Des,* vol. 50, pp. 253-266, 2013.

[15] T. Uemori, S. Susmikawa, T. Naka, N. Ma, and F. Yoshida, "Influence of Bauschinger Effect and anisotropy on springback of aluminum alloy sheets," *Mater. Trans.,* vol. 58, no. 6, pp. 921-926, 2017.

[16] W. Julsri, S. Suranuntchai, and V. Uthaisangsuk, "Study of springback effect of AHS steels using a microstructure based modeling," *Int. J. Mech. Sci.,* vol. 135, pp. 499-516, 2018.

[17] F. Yoshida and T. Uemori, "A model of large-strain cyclic plasticity describing the Bauschinger effect and workhardening stagnation," *Int J Plast,* vol. 18, pp. 661-686, 2002.

[18] N. Brinis, B. Regaiguia, O. Chahaoui, N. Maatougui, and M. L. Fares, "Modelling mechanical properties of AISI 439-430Ti ferritic stainless steel sheet," *J. Solid Mech.,* vol. 11, no. 2, pp. 425 - 439, 2019.

[19] J.-W. Lee, F. Barlat, and D.-J. Kim, "Sheet forming simulations of automotive parts using different yield functions," in *NUMIFORM 2010*, F. Barlat, Y. H. Moon, and M. G. Lee, Eds., June 01, 2010 2010, vol. 1252: AIP, pp. 361-368.

[20] Y. Hou, X. L. Zhang, J. Y. Min, and M. G. Lee, "Plastic deformation of ultra-thin pure titanium sheet subject to tension-compression loadings," *IOP Conf. Ser. Mater. Sci. Eng.,* vol. 1270, no. 1, p. 012020, 2022.

[21] F. Barlat *et al.*, "Plane stress yield function for aluminum alloy sheets—part 1: theory," *Int J Plast,* vol. 19, no. 9, pp. 1297-1319, 2003.

[22] O. Chahaoui, N. Matougui, S. Boulahrouz, M. Heddar, and K. Babouri, "An associated and nonassociated flow rule comparison for AISI 439-430TI forming: Modeling and experimental analysis," *LAJSS,* vol. 18, 2021.

[23] R. Hill, "A theory of the yielding and plastic flow of anisotropic metals," *Proc. R. Soc. Lond. A,* vol. 193, pp. 281–297, 1948.

[24] J. Lian *et al.*, "An evolving non-associated Hill48 plasticity model accounting for anisotropic hardening and r-value evolution and its application to forming limit prediction," *Int J Solids Struct,* vol. 151, pp. 20-44, 2018.

[25] F. Barlat and K. Lian, "Plastic behavior and stretchability of sheet metals. Part I: A yield function for orthotropic sheets under plane stress conditions," *Int J Plast,* Article vol. 5, no. 1, pp. 51-66, 1989.

[26] F. Barlat and O. Richmond, "Prediction of tricomponent plane stress yield surfaces and associated flow and failure behavior of strongly textured f.c.c. polycrystalline sheets," *Mater. Sci. Eng.,* Article vol. 95, no. C, pp. 15-29, 1987.

[27] D. Banabic, "Plastic behaviour of sheet metal," in *Sheet Metal Forming Processes: Constitutive Modelling and Numerical Simulation*, 1 ed.: Springer Berlin Heidelberg, 2010, ch. 2, sec. 2.3, pp. 45-75.
[28] F. Barlat *et al.*, "Yield function development for aluminum alloy sheets," *J. Mech. Phys. Solids,* Article vol. 45, no. 11-12, pp. 1727-1763, 1997.
[29] A. P. Karafillis and M. C. Boyce, "A general anisotropic yield criterion using bounds and a transformation weighting tensor," *J. Mech. Phys. Solids,* Article vol. 41, no. 12, pp. 1859-1886, 1993.
[30] F. Barlat, H. Aretz, J. W. Yoon, M. E. Karabin, J. C. Brem, and R. E. Dick, "Linear transfomation-based anisotropic yield functions," *Int J Plast,* Article vol. 21, no. 5, pp. 1009-1039, 2005.
[31] R. D. Krieg, "A practical two surface plasticity theory," *J Appl Mech,* Article vol. 42, no. 3, pp. 641-646, 1975.
[32] F. Yoshida and T. Uemori, "A model of large-strain cyclic plasticity and its application to springback simulation," *Int. J. Mech. Sci.,* vol. 45, pp. 1687-1702, 2003.
[33] F. Yoshida, T. Uemori, and K. Fujiwara, "Elastic-plastic behavior of steel sheets under in-plane cyclic tension-compression at large strain," *Int J Plast,* vol. 18, pp. 633-659, 2002.
[34] *Standard Test Methods for Tension Testing of Metallic Materials*, ASTM International Standard No. ASTM E8, American Society for Testing Materials (ASTM), West Conshohocken, PA, 2016
[35] *Standard Test Method for Plastic Strain Ratio r for Sheet Metal*, ASTM International Standard No. ASTM E517-00, American Society for Testing Materials (ASTM), West Conshohocken, PA, 2017
[36] S. Luksanayam, "Formability study on high strength steel NSC980D automotive parts using forming limit diagram," Master's Thesis, Tool and Materials Engineering, King Mongkut's University of Technology Thonburi, Bangkok, 2018.
[37] *Metallic Materials — Sheet and Strip — Determination of Forming-Limit Curves—Part 2: Determination of Forming-Limit Curves in the Laboratory*, ISO12004-2:2008, International Organization for Standardization (ISO), Geneva, Switzerland, 2008
[38] *Testing and Documentation Guideline for the Experimental Determination of Mechanical Properties of Steel Sheets for CAE-Calculations*, SEP 1240:2006-07, STAHL, Germany, 2006
[39] S. Panich, F. Barlat, V. Uthaisangsuk, S. Suranuntchai, and S. Jirathearanat, "Forming limit curves and forming limit stress curves for advanced high strength steels," *Materials Science Forum,* vol. 773–774, pp. 109–114, 2013.
[40] T. Jantarasricha, S. Panich, and K. Chongbunwatana, "Development of stress- and strain-based fracture forming limit curves of sheet aluminium-alloy AA2024-T3 through various approaches," *KEM,* vol. 856, no. 856, pp. 57-65, 2020.
[41] ESI Group, "Blank," *vol. I*, *PAM-STAMP 2019 user's guide*: ESI Group, 2019, pp. 334-339.
[42] A. Güner, C. Soyarslan, A. Brosius, and A. E. Tekkaya, "Characterization of anisotropy of sheet metals employing inhomogeneous strain fields for Yld2000-2D yield function," *Int J Solids Struct,* vol. 49, no. 25, pp. 3517-3527, 2012.
[43] D. Banabic and M. Sester, "Influence of material models on the accuracy of the sheet forming simulation," *Mater. Manuf. Process.,* vol. 27, no. 3, pp. 273–277, 2012.
[44] J. W. Yoon, F. Barlat, K. Chung, F. Pourboghrat, and D. Y. Yang, "Earing predictions based on asymmetric nonquadratic yield function," *Int J Plast,* Article vol. 16, no. 9, pp. 1075-1104, 2000.
[45] S. Basak and S. K. Panda, "Implementation of Yld96 anisotropy plasticity theory for estimation of polar effective plastic strain based failure limit of pre-strained thin steels," *Thin-Walled Struct,* Article vol. 126, pp. 26-37, 2018.
[46] B. Regaiguia, O. Chahaoui, S. Boulahrouz, N. Brinis, and M. L. Fares, "Constitutive modelling of an industrial rolled sheet for a DIN 1623 St14 (DC04) Steel," *SSP,* vol. 297, pp. 31-50, 2019.

Chanatip Tonglamool, photograph and biography not available at the time of publication.

Surasak Suranuntchai, photograph and biography not available at the time of publication.